



Published in final edited form as:

*Phys Med Biol.* ; 63(6): 065009. doi:10.1088/1361-6560/aab05c.

## Power cavitation-guided blood-brain barrier opening with focused ultrasound and microbubbles

M T Burgess<sup>1</sup>, I Apostolakis<sup>1</sup>, and E E Konofagou<sup>1,2</sup>

<sup>1</sup>Department of Biomedical Engineering, Columbia University, New York, NY, USA

<sup>2</sup>Department of Radiology, Columbia University, New York, NY, USA

### Abstract

Image-guided monitoring of microbubble-based focused ultrasound (FUS) therapies relies on the accurate localization of FUS-stimulated microbubble activity (*i.e.* acoustic cavitation). Passive cavitation imaging with ultrasound arrays can achieve this, but with insufficient spatial resolution. In this study, we address this limitation and perform high-resolution monitoring of acoustic cavitation-mediated blood-brain barrier (BBB) opening with a new technique called power cavitation imaging. By synchronizing the FUS transmit and passive receive acquisition, high-resolution passive cavitation imaging was achieved by using delay and sum (DAS) beamforming with absolute time delays. Since the axial image resolution is now dependent on the duration of the received acoustic cavitation emission, short pulses of FUS were used to limit its duration. Image sets were acquired at high-frame rates for calculation of power cavitation images analogous to power Doppler imaging. Power cavitation imaging displays the mean intensity of acoustic cavitation over time and was correlated with areas of acoustic cavitation-induced BBB opening. Power cavitation-guided BBB opening with FUS could constitute a standalone system that may not require MRI guidance during the procedure. The same technique can be used for other acoustic cavitation-based FUS therapies, for both safety and guidance.

### Keywords

focused ultrasound; beamforming; acoustic cavitation; image-guided therapy; blood-brain barrier

### 1. Introduction

Blood-brain barrier (BBB) opening with focused ultrasound (FUS) and microbubbles is a promising drug delivery strategy for treatment of neurological diseases such as Parkinson's, Alzheimer's, and brain cancer (Leinenga et al., 2016). This technique harnesses the mechanical bioeffects of ultrasound-stimulated microbubble activity (*i.e.* acoustic cavitation) to temporarily compromise the integrity of the BBB for diffusion of drugs into the brain parenchyma that would otherwise be impermeable (Hynynen et al., 2001; Choi et al., 2007; Tung et al., 2011). By using FUS to restrict acoustic cavitation to a defined focal volume, BBB opening can be achieved in specific regions of the brain in order to facilitate targeted drug delivery. Numerous studies in mice and non-human primates have shown that transcranial FUS, along with intravenously injected microbubbles, is a safe, repeatable way to temporarily open the BBB for delivery of a wide range of drugs, such as antibodies,

nanoparticles, proteins, and viral vectors (Timbie et al., 2015; Downs et al., 2015; Baseri et al., 2010). Additionally, BBB opening alone has been shown to stimulate an immunological response in the brain to ameliorate neurological disease progression, therefore serving as a non-pharmacological treatment modality (Leinenga and Götz, 2015). As the only truly non-invasive, transient, and targeted method for BBB opening, research interest has stimulated the development of image-guided FUS systems. Magnetic resonance imaging-guided FUS (MRIgFUS) has been the gold standard due to its high image quality and current implementation for high-intensity FUS temperature monitoring during thermal ablation (Hynynen, 2011). However, its high cost, lack of portability, long treatment times, and inability to monitor acoustic cavitation-based FUS therapies limits the enthusiasm of MRIgFUS for BBB opening. Ultrasound-guided FUS (USgFUS) systems, stand-alone or in combination with MRI, have the ability to address these limitations (Arvanitis et al., 2013; Wei et al., 2013; Crake et al., 2017).

Acoustic cavitation detection is the principal strategy to guide and monitor BBB opening with FUS and microbubbles (Tung et al., 2011; Arvanitis et al., 2012; O'Reilly and Hynynen, 2012; Wu et al., 2014; Sun et al., 2015; Tsai et al., 2016; Sun et al., 2017). Incident ultrasound energy on a microbubble is absorbed, leading to volumetric oscillations and radiation of secondary acoustic emissions by the microbubble (Hilgenfeldt et al., 1998). These active secondary emissions can be detected and carry important spectral and temporal information about the microbubble dynamics in the vascular space. Harmonic, sub-harmonic, and ultra-harmonic content (relative to the driving frequency) is associated with repetitive, non-linear oscillations of the microbubble around an equilibrium size (i.e. stable cavitation), while increased broadband content is indicative of microbubble collapse (i.e. inertial cavitation). Together, these spectral components can be monitored to gauge the intensity of acoustic cavitation and therefore the degree of bioeffects leading to BBB opening. Single-element and multi-element transducers have been used as passive cavitation detectors. Single-element transducers are sufficient to measure acoustic cavitation emissions within their fixed receive sensitivity patterns, which is typically confocal with the FUS transducer. Therefore, they provide bulk measurements of acoustic cavitation emissions emanating from the focal volume, but lack the ability to resolve the spatial distribution of activity. To overcome this limitation, multi-element arrays (i.e. ultrasound imaging arrays) have been implemented to record acoustic cavitation emissions and beamform them to their spatial points of origin. Termed passive cavitation imaging or passive acoustic mapping, this technique has been used to monitor numerous USgFUS therapies, such as targeted drug delivery (Choi et al., 2014; Kwan et al., 2015; Haworth et al., 2016), thermal ablation (Gyöngy and Coussios, 2010b; Arvanitis and McDannold, 2013; Haworth et al., 2015), and histotripsy (Bader et al., 2017). In addition, passive cavitation imaging has been used to understand acoustic cavitation dynamics (Gyöngy and Coussios, 2010a; Choi and Coussios, 2012; O'Reilly et al., 2014; Crake et al., 2015; Pouliopoulos et al., 2015) and been modified for transcranial imaging using aberration correction (Arvanitis et al., 2015; Jones et al., 2015).

Initially developed for spatial mapping of acoustic cavitation during thermal ablation with FUS, the beamforming for passive cavitation imaging is based on time exposure acoustics (Norton and Won, 2000; Gyöngy et al., 2008; Gyöngy and Coussios, 2010b). Since HIFU

exposures are continuous wave and acoustic cavitation events occur at random throughout the exposure duration, conventional pulse-echo beamforming techniques cannot be used since absolute time of flight information is lost. Therefore, Gyöngy and Coussios (2010b) assumed acoustic cavitation events are fixed point sources that radiate spherical wavefronts to the imaging array. By using relative differences in the time of arrival between elements in the array, the cavitation events can be spatially mapped using a delay, sum, and integrate (DSAI) beamforming approach (Gyöngy et al., 2008; Salgaonkar et al., 2009; Farny et al., 2009). This methodology has been implemented using both time and frequency domain approaches to create images of acoustic cavitation activity that distinguish the type of cavitation (*i.e.* stable or inertial) and its location (Gyöngy and Coussios, 2010b; Haworth et al., 2012; Haworth et al., 2017; Arvanitis et al., 2017).

The resolution of passive cavitation imaging using DSAI beamforming is determined by the diffraction pattern of the receive array and not the duration of the received echo as with conventional B-mode ultrasound imaging (Gyöngy and Coussios, 2010b; Salgaonkar et al., 2009; Haworth et al., 2017; Gateau et al., 2011). For typical diagnostic imaging arrays employed for passive cavitation imaging, this severely limits the axial resolution and consequently the utility of this technique for monitoring FUS therapies. An alternative strategy for pulsed wave FUS therapies is to synchronize the FUS transmit with the receive acquisition. If short pulses of FUS are used to limit the duration of acoustic cavitation activity, conventional delay and sum (DAS) beamforming can be used to improve the axial resolution (Gateau et al., 2011). In this scenario, the FUS transmit and receive acquisition are synchronized to preserve absolute time of flight information and therefore localize cavitation events in time and space. This is the major distinction from DSAI beamforming, which can only localize events in space. Instead of integrating the beamformed signal for each pixel, DAS beamforming uses absolute time of flight information to time gate the signal and isolate emissions originating from certain points in the imaging field of view.

In this study, we implement synchronized passive cavitation imaging with DAS beamforming to monitor transcranial BBB opening with FUS and microbubbles in a mouse. We hypothesize that by using short pulses of FUS, we can restrict the duration of acoustic cavitation emissions and therefore obtain sufficient axial image resolution for monitoring. Since the beamforming is now equivalent to conventional methods used for B-mode ultrasound imaging, techniques from contrast-enhanced ultrasound imaging and high-frame rate imaging can be used to further increase the image resolution and isolate non-linear acoustic cavitation emissions. Furthermore, we introduce a new concept called power cavitation imaging, where sets of passive cavitation images acquired at high-frame rates can be processed in a manner analogous to power Doppler imaging. In this case, the mean intensity image, or power cavitation image, reveals the spatial distribution of acoustic cavitation intensity throughout the focal area of the FUS transducer. This information can be used to predict areas with significant levels of acoustic cavitation-mediated bioeffects. The sections below will outline the methods and results for this study and discuss the potential of this technique for monitoring FUS-mediated BBB opening and other acoustic cavitation-based therapies.

## 2. Methods

### 2.1. Animals

This study was performed in accordance to the Institutional Animal Care and Use Committee (IACUC) at Columbia University. One female mouse (Weight: 22.6 g, C57BL/6, Harlan Sprague Dawley Inc., Indianapolis, IN, USA) was used for this proof of concept experiment. The mouse was anesthetized with a mixture of oxygen and 1.0–2.0% vaporized isoflurane (0.8 L/min) during the treatment. Depilatory cream was used to remove hair from the scalp and the mouse was positioned in a stereotaxic instrument (Model 900, David Kopf Instruments, Tujunga, CA, USA).

### 2.2. Experimental setup

Passive cavitation imaging was performed using a dual transducer setup as shown in Figure 1A. A 1-MHz, 0.5-inch diameter FUS transducer (A303S, Olympus America Inc., Waltham, MA, USA) with a 20-mm spherical focus was angled off-axis relative to an 18-MHz high frequency linear array (L22-14v Long Focus, –6 dB bandwidth: 12.6 – 24.8 MHz, Verasonics Inc., Kirkland, WA). The 20-mm elevation focus of the linear array was aligned with the 20-mm geometric focus of the 1-MHz transducer using a custom transducer holder. A waveform generator (Keysight Technologies Inc., Santa Rose, CA, USA) and RF power amplifier (Electronics & Innovation Ltd., Rochester, NY, USA) were used to drive the 1-MHz FUS transducer. A research ultrasound system (Vantage 256, Verasonics Inc., Kirkland, WA, USA) was used to acquire passive acoustic cavitation emissions and synchronize the FUS transmit with the receive acquisition of the imaging array. This was achieved by externally triggering the waveform generator at the beginning of each receive acquisition using the trigger out capability of the ultrasound system. The waveform generator was operated in externally triggered burst mode using a one-cycle sine wave at 1 MHz. The pulse repetition rate (PRF) was set by the interframe acquisition time on the ultrasound system. Free-field pressure measurements were made using a capsule hydrophone (HGL-0200, Onda Corporation, Sunnyvale, CA, USA) to calibrate the peak negative pressure (PNP) output of the 1-MHz FUS transducer and measure its waveform and axial pressure field as shown in Figure 1C and Figure 1D, respectively. Due to the narrow bandwidth of the FUS transducer, the actual waveform was longer than one cycle.

### 2.3. Microbubbles

Size-isolated, lipid-coated microbubbles in the 4–5  $\mu\text{m}$  diameter range were manufactured using a previously published protocol (Feshitan et al., 2009). Briefly, lipids 1,2-distearoyl-sn-glycero-3-phosphocholine (DSPC, Avanti Polar Lipids Inc., Alabaster, AL, USA) and 1,2-distearoyl-sn-glycero-3-phosphoethanolamine-N-[methoxy(polyethylene glycol)-2000] (DSPC-mPEG2000, Avanti Polar Lipids Inc., Alabaster, AL, USA) were weighted out in a glass vial at a 9:1 DSPC: DSPC-mPEG2000 molar ratio. The lipids were then dissolved in a 50-mL mixture of 10-vol % glycerin, 10-vol % propylene glycol, and 80-vol % phosphate-buffered saline and heated to 60°C. The solution was placed in a 60°C sonication bath for 1-2 hours and then sonicated with a high-power sonication tip for 10 minutes to produce a clear suspension at a lipid concentration of 2 mg/mL. Microbubbles were created by streaming perfluorobutane (FluoroMed L.P., Round Rock, TX, USA) gas into the head space

of the lipid suspension and sonicating with a high-power sonication tip. The microbubble suspension was collected into 30-mL syringes and all microbubbles were separated by centrifuging at 300 relative centrifugal force (RCF) for 3 minutes using a swing-bucket rotor centrifuge (Eppendorf, Hauppauge, NY, USA). Size-isolated microbubbles in the 4-5  $\mu\text{m}$  diameter range were then collected using the methods described by Feshitan et al. (2009). A Multisizer III particle counter (Beckman Coulter Life Sciences, Indianapolis, IN, USA) was used to measure the size and concentration of microbubbles.

#### 2.4. Passive Cavitation Imaging

Passive cavitation imaging with DAS or DSAI beamforming was carried out using the notation and image geometry shown in Figure 1B. The origin of the FUS wave and image axes was set to the center of the FUS transducer aperture. The time of flight the FUS wave was defined by two path lengths: (1) the time to travel from the line tangent to the apex of the FUS transducer aperture to a given pixel coordinate  $(x, z)$  in the imaging field of view:

$$t_1(x, z) = (z\cos\alpha + x\sin\alpha)/c \quad (1)$$

and (2) the travel time to the  $n$ th-element position  $(x_n, z_0)$  in the imaging array:

$$t_{2,n}(x, z) = \sqrt{(z + z_0)^2 + (x - x_n)^2}/c \quad (2)$$

where  $\alpha$  is the angle between the FUS transducer and imaging array,  $z_0$  is the z-axis standoff distance of the imaging array relative to the FUS transducer,  $x_n$  is the lateral position of the  $n$ th-element, and  $c$  is the sound speed. The absolute time delay to the  $n$ th-element,  $\tau_{abs,n}$  is defined as the two way travel time:

$$\tau_{abs,n} = t_1 + t_{2,n} \quad (3)$$

For a given FUS transmit, the imaging array was operated in a receive-only mode to acquire passive acoustic emissions emanating from the imaging field of view. Data was captured on all 128 elements of the receive array and bandpass filtered ( $-20$  dB stopband points: 12 and 25 MHz) after pre-amplification and A/D conversion. The received data was then stored in the buffer on the ultrasound system. For each received radio frequency (RF) data set acquisition,  $N$ -total frames were accumulated into the buffer at high-frame rates before transfer to the host computer for saving. Image reconstruction was performed off-line using a graphics processing unit (GPU)-accelerated (Tesla C2075, Nvidia, Santa Clara, CA, USA) beamforming algorithm based on the DAS method (Montaldo et al., 2009). For each pixel position, the absolute time delays were calculated for the  $n$ th-element position in the imaging array. The received RF data,  $RF(n, t)$ , was then beamformed to each pixel location by time delaying the RF data and summing up the contributions from each element. The beamformed RF data for the  $m$ th-frame using absolute time delays is defined as:

$$s_{abs,m}(x, z) = \left| \sum_{n=1}^{128} RF(n, \tau_{abs,n}(x, z)) \right|^2 \quad (4)$$

This set of RF data is processed together to produce a single power cavitation image,  $S(x, z)$ , defined as:

$$S(x, z) = \frac{1}{N} \sum_{m=1}^N |s_{abs,m}(x, z)|^2 \quad (5)$$

where  $s_{abs,m}(x, z)$  is the  $m$ th-beamformed frame of received RF data and  $N$  is the total number of frames. The intensity envelope of each beamformed frame was taken and log-compressed relative to the maximum pixel intensity prior to image formation. All images were created with pixel spacing of a  $\lambda$  in the x-dimension and  $\lambda/2$  in the z-dimension relative to 18 MHz. For comparison of DAS beamforming with absolute time delays to previous methods, an individual frame of received RF data was processed using the DSAI beamforming algorithm described by Haworth et al. (2017). The relative time delay for the  $n$ th-element,  $\tau_{rel,m}$  is defined as the relative difference in time of arrival between elements:

$$\tau_{rel,m} = t_{2,n} - \left( \frac{z + z_0}{c} \right) \quad (6)$$

The beamformed RF data using DSAI beamforming with relative time delays is defined as:

$$s_{rel}(x, z) = \int_{t_i}^{t_f} \left| \sum_{n=1}^{128} RF(n, t + \tau_{rel,n}(x, z)) \right|^2 dt \quad (7)$$

where  $t_i$  and  $t_f$  is the start and end time of the received RF data acquisition, respectively. The entire duration of received RF data was used for beamforming (*i.e.*  $t_f - t_i = 25 \mu s$ ) and integration was performed using all frequencies within the bandwidth of the imaging array.

## 2.5. In-vitro experiments

Proof of concept experiments were performed in a two-liter tank of deionized water containing microbubbles. This was used to isolate microbubble-specific acoustic emissions to illustrate the functionality of this technique. Microbubbles were added at a concentration of approximately 2000 microbubbles/mL and continually mixed throughout the experiment. The dual transducer setup was partially submerged into the tank and received RF data sets were acquired at a PRF of 100 Hz using the FUS pulse in Figure 1C at 280 kPa PNP. For each acquisition, 100 total frames of received RF data was accumulated into the buffer and then saved to the host PC. This was repeated 100 times for a total 10,000 individual frames, with an approximate one second delay between each 100 frame acquisition for saving. For a

detailed comparison between the different beamforming algorithms described in Section 2.4, the microbubbles were further diluted to acquire single microbubble echoes.

## 2.6. Monitoring of BBB opening with power cavitation imaging

The dual transducer setup was immersed into a small tank of degassed, deionized water positioned above the head of the mouse. B-mode ultrasound imaging was performed to place the FUS focal area approximately 2 mm anterior of the lambda suture and 2 mm below the skull using a three-axis positioning system (Velmex Inc., Bloomfield, NY, USA). The FUS parameters used for BBB opening were the same as in vitro experiments (280 kPa PNP measurement in free field), except the received RF data was acquired at a PRF of 1000 Hz. For each receive acquisition, 200 frames of RF data were accumulated into the buffer and then saved to the host PC. The save time was approximately three seconds between acquisitions and there was a total of 300 acquisitions. At approximately the 20<sup>th</sup> and 150<sup>th</sup> acquisition, a 1  $\mu\text{L/g}$  bolus injection of microbubbles was administered from a diluted microbubble solution containing  $8 \times 10^8$  microbubbles/mL in saline.

## 2.7. MRI

Contrast-enhanced MRI was performed after FUS exposure to confirm BBB opening and compare with power cavitation images. Immediately after the exposure, a bolus injection of 0.2 mL of gadodiamide (Omniscan, GE Healthcare, Princeton, NJ, USA) was administered intraperitoneally. Approximately 30 minutes after injection, the mouse was anesthetized and placed in a 3 cm diameter birdcage coil inside the vertical bore of the MRI system. A 9.4 T MRI system (DRX400, Bruker Medical, Billerica, MA, USA) was used to perform a T1-weighted 2D FLASH sequence (Repetition Time: 230 ms, Echo Time: 3.3 ms, Flip Angle: 70°, 6 averages, Field of View (FOV): 25.6 mm  $\times$  25.6 mm, Matrix Size: 256  $\times$  256, Slice Thickness: 400  $\mu\text{m}$ , Resolution: 100  $\mu\text{m}$   $\times$  100  $\mu\text{m}$ ).

## 3. Results

### 3.1. In vitro experiments: beamforming comparison

Initial experiments using passive cavitation imaging were performed in a microbubble suspension for free-field reception of acoustic cavitation emissions. The purpose of these experiments was to isolate echoes from individual microbubbles moving freely throughout the focal area. A received RF data set with a limited number of acoustic cavitation events was captured for comparison of the different beamforming methods. Figure 2A is the received RF data showing the wavefront from the strongest microbubble source located at a  $(x, z)$  coordinate of approximately (16 mm, 21 mm). Figure 2B is the delayed RF data and Figure 2C is the delayed and summed (beamformed) RF signal for the pixel located at the strongest microbubble source. Figure 2D is the corresponding power spectrum of the beamformed RF signal. Lastly, Figure 2E is the passive cavitation image using DAS with absolute time delays and Figure 2F is the passive cavitation image using DSAI with relative time delays. Figure 2E and 2F were plotted with different dynamic ranges due to different signal-to-noise ratios (SNR). The noise floor can be seen in both images, which was approximately  $-31.2$  dB ( $\pm 5$  dB) relative to maximum pixel intensity for Figure 2E and approximately  $-8.8$  dB ( $\pm 0.3$  dB) relative to maximum pixel intensity for Figure 2F. The

low SNR of the DSAI passive cavitation image is due to the integration of a brief echo (approximately  $0.3 \mu\text{s}$ ) over a long acquisition duration ( $t_f - t_i = 25 \mu\text{s}$ ).

It is important to note that both the absolute and relative time delays for this pixel position would produce the same effect of flattening the wavefront curvature. The main difference between DAS and DSAI beamforming arises from the processing of the beamformed RF signal. DAS with absolute time delays has the advantage of knowing when the emission should occur in time for a given pixel position based on absolute time of flight calculation in Equation 3. Therefore, the beamformed signal can be time gated (*i.e.* depth gated using the speed of sound) when assigning the amplitude from the beamformed RF signal to the pixel's brightness value. DSAI beamforming does not use additional information related to when emissions are occurring relative to the transmit and receive acquisition. Instead, DSAI beamforming integrates the beamformed RF signal over the entire acquisition length (*i.e.* from all depths). If an emission was present during that time, DSAI spatially maps the energy of that emission to the corresponding pixel by using relative time delays. A quantitative comparison of the image resolution between Figure 2E and Figure 2F was performed by measuring the point spread function of the two images. This was done by measuring the  $-3$  dB full width of the microbubble source located at (16 mm, 21 mm) in both the axial and lateral directions. The  $-3$  dB axial width was approximately  $150 \mu\text{m}$  using DAS and approximately 2 mm using DSAI. The  $-3$  dB lateral width of the source was approximately  $200 \mu\text{m}$  for both beamforming methods.

### 3.2. In vitro experiments: power cavitation imaging of a microbubble suspension

Figure 3 shows the process for generating power cavitation images from a microbubble suspension. Figure 3A are the individual passive cavitation images acquired at a frame rate of 100 Hz. Figure 3B shows the resultant power cavitation images from each 100 frame acquisition using Equation 5 and the mean power cavitation is shown in Figure 3C, which is the mean image calculated from 100 power cavitation images (10,000 passive cavitation images). Lastly, Supplementary Video 1 displays the first 500 passive cavitation images and corresponding power cavitation image as the total number of frames,  $N$ , increases and updates the power cavitation image calculation as shown in Equation 5. The mean power cavitation image reveals the varying intensity and occurrence of acoustic cavitation events throughout the focal area. Acoustic cavitation events were only detected within the focal beam shape of the FUS transducer. During the experiment, the microbubble suspension was vigorously mixed to ensure a similar number of acoustic cavitation events were detected throughout the focal area. If we assume that the roughly the same number events were detected at each pixel coordinate throughout the focus, it can be hypothesized that the varying intensity of the image is related to the diffraction pattern of the FUS beam as shown in Figure 1D. Since the acoustic pressure varies gradually throughout the focal area, microbubbles closer to the focal point act as stronger sources than those located just outside.

### 3.3. In vivo application: monitoring of blood-brain barrier opening with power cavitation imaging

Figure 4 shows the results of using power cavitation imaging to monitor transcranial BBB opening with FUS and microbubbles in a mouse. Figure 4A are the individual passive

cavitation images acquired at a 1000 Hz frame rate. Figure 4B is the power cavitation image calculated from a single 200 frame set of passive cavitation images. Figure 4C is the intensity of the pixel located at a  $(x, z)$  coordinate of approximately (28 mm, 18 mm) over the 0.2 second acquisition. In general, the intensity of acoustic cavitation was highest at the beginning of each acquisition and then decreased to a constant value. This peak of activity is hypothesized to arise from the initial destruction of microbubbles in the focal area, followed by a steady replenishment of activity from new microbubbles flowing into the area.

Individual power cavitation images are shown in Figure 4D, which were calculated from each 200 frame set of passive cavitation images over the entire treatment duration. The mean power cavitation image is shown in Figure 4E, which was determined from the 300 power cavitation images acquired over the treatment duration. Figure 4F is the pixel intensity of the power cavitation images over time at a  $(x, z)$  coordinate of approximately (28 mm, 19.5 mm). Lastly, Supplementary Video 2 shows the individual power cavitation images over the entire treatment duration. Compared to the uniform distribution of microbubble activity as seen in Figure 3C, *in vivo* power cavitation images revealed a spatially varied distribution of acoustic cavitation activity throughout the focal area due to the underlying microvasculature. Significant acoustic cavitation activity can be seen in the cerebral cortex and subcortical areas of the left hemisphere of the mouse brain. Figure 4F captures important information related to the infusion dynamics and persistence of acoustic cavitation within the focal area. No activity was detected until microbubble injection at approximately 60 seconds, where significant amounts of acoustic cavitation activity were detected that slowly decreased until the second injection at approximately 460 seconds. Figure 5 compares the mean power cavitation image with the contrast-enhanced MRI taken after BBB opening. As seen in Figure 5B, significant contrast leakage is seen in the cerebral cortex and subcortical areas of the left hemispheres that correlates with the intense areas of acoustic cavitation activity in Figure 5A, which is overlaid on the B-mode image.

#### 4. Discussion

This study combines concepts from passive cavitation imaging, contrast-enhanced ultrasound imaging, and high-frame rate Doppler imaging to create an innovative approach for monitoring of acoustic cavitation-mediated BBB opening with FUS and microbubbles. We show that the axial resolution of passive cavitation imaging can be improved by using conventional DAS beamforming with absolute time delays and short pulses of FUS. In this case, the axial resolution is mainly dependent on the duration of the received acoustic cavitation signals. Conceptually, this can be thought of as B-mode imaging with focused beam transmits originating from the FUS transducer. A limited section of the imaging field of view is interrogated with the FUS beam and echoes from within the beam area are passively received using the imaging array. Since the geometry is fixed, it is easy to adjust the time delays to account for the imaging pulse originating from the FUS transducer and not the imaging array. Therefore, the received RF data can be dynamically focused to each pixel in the image field of view using DAS beamforming.

The main advantage of the experimental setup used in this study, is that the imaging array is only sensitive to echoes from microbubbles, *i.e.* acoustic cavitation. This type of transducer

arrangement is similar to the non-linear ultrasound imaging mode sensitive to broadband acoustic emissions from microbubbles (Kruse and Ferrara, 2005). Kruse and Ferrara (2005) demonstrated the use of this technique for highly sensitive imaging of microbubbles with two transducers separated in frequency. The imaging technique excites microbubbles with a lower frequency FUS pulse and images the non-linear acoustic emissions with a higher frequency imaging array. The FUS pulse causes the microbubbles to undergo inertial cavitation, where the microbubbles grow to some maximum radius and then collapse due to the inertia of the intruding fluid. Upon collapse to some minimum radius, a shock wave or pressure spike is emitted that is broadband in the frequency domain. While it is assumed that the microbubble also scatters energy at the frequency components in the FUS pulse, the imaging array is only sensitive to the high frequency content contained within the pressure spike. The imaging array used in this study has a frequency bandwidth ( $-6$  dB width: 12.6 – 24.8 MHz) well above the primary FUS frequency (1 MHz). This allows the imaging array to act as a natural filter and reduce imaging sensitivity towards scattering at the FUS frequency and associated harmonics due to non-linear wave propagation. Therefore, the high frequency content in the collapse spikes can be detected and imaged with resolution defined by the imaging array frequency and not the FUS frequency. This is clearly shown by comparing the durations of the FUS pulse and beamformed RF signal in Figure 1C and Figure 2C, respectively. The duration of the FUS pulse is approximately  $4 \mu\text{s}$ , while the duration of the beamformed RF signal is approximately  $0.3 \mu\text{s}$ . This highlights the super resolution aspect of this non-linear imaging mode since the spatial length of the beamformed RF signal is subwavelength relative to the 1-MHz FUS pulse. Recent research has taken advantage of this contrast-enhanced imaging mode for molecular imaging and assessment of tumor microvasculature (Hu et al., 2014; Gessner et al., 2013; Ma et al., 2014). Other researchers have explored the use of this non-linear acoustic emission for determining the inertial cavitation threshold of ultrasound contrast agents (Ammi et al., 2006).

Since acoustic cavitation is originating from microbubbles in the blood, specialized processing techniques developed for Doppler imaging can be used to more effectively visualize acoustic cavitation activity over time. Doppler imaging tracks the backscattered energy from red blood cells over time using successive B-mode image frames. The brightness of each pixel over consecutive frames, *i.e.* Doppler signal, can be filtered and analyzed to extract information about the axial blood velocity (color Doppler) and blood volume (power Doppler) (Mace et al., 2013). Instead of processing a stack of B-mode ultrasound images, a stack of passive cavitation images can also be analyzed in this manner. In this study, passive cavitation images are formed from received RF data that contains only acoustic cavitation emissions. The brightness of each pixel over successive passive cavitation image frames, *i.e.* cavitation signal, can be processed to provide information related to the intensity of acoustic cavitation activity over time. The mean intensity of the cavitation signals for all pixels, *i.e.* power cavitation image, is analogous to power Doppler imaging and proportional to the number of acoustic cavitation events and their emission strength. Due to the improved image resolution with DAS beamforming using absolute time delays, power cavitation images can provide important information in regards to the distribution of acoustic cavitation activity throughout the focal area due to the underlying vasculature. Additionally, spatiotemporal clutter filtering techniques developed for ultrafast

Doppler imaging can be used to eliminate stationary tissue scatter and isolate rapidly changing microbubble emissions in the blood (Demené et al., 2015). This will be particularly important for scenarios where the FUS frequency and imaging array bandwidth overlap. Although no filtering was needed for this study since the FUS and imaging frequencies were far apart, we surmise that clutter filtering will be a useful tool to improve the applicability and sensitivity of power cavitation imaging. Arnal et al. (2017) demonstrated the potential of spatiotemporal filtering during active cavitation imaging of bubble clouds with ultrafast diverging waves. By using the singular value decomposition (SVD) method, they were able to isolate the spatiotemporal characteristics of bubble clouds and greatly improve the cavitation image contrast.

The main limitation of this technique lies in the FUS pulse length. Therefore, it is suited for FUS therapies that can use pulse designs similar to broadband diagnostic imaging. With increasing pulse lengths, the duration of the received echoes will increase, leading to a reduction in axial resolution. In relation to the non-linear imaging mode used in this study, longer FUS pulses will also cause microbubbles to undergo numerous growth and collapse cycles, with the emission of multiple pressure spikes separated by the period of the FUS frequency. This will lead to the appearance of phantom microbubble sources in the image, where a single microbubble will appear as multiple microbubbles spaced vertically on the image. Each successive collapse occurs later in time and thus will appear below the previous collapse on the image, separated by wavelength of the FUS frequency. However, the technique is not limited to imaging of inertial cavitation. Other non-linear imaging modes, such as pulse-inversion and subharmonic imaging, can be used to detect non-linear emissions related to stable cavitation (Simpson et al., 1999; Chomas et al., 2002). In theory, this method would also work for fundamental mode imaging, since the fast moving echoes from microbubbles insonified in the focal area can be isolated from slow moving tissue motion using the aforementioned spatiotemporal clutter filtering. Acoustic cavitation-based FUS therapies that require longer pulses would benefit from passive cavitation imaging with DSAI beamforming. This technique may provide increased SNR since the beamformed RF signal is integrated over time, although a similar effect is achieved by accumulation of consecutive passive cavitation images acquired at high-frame rates using DAS beamforming. Additionally, DSAI beamforming does not depend on precise registration of the imaging array relative to the FUS transducer for calculations of time delays. This gives the user flexibility in the alignment strategy at the cost of resolution depending upon the orientation (Haworth et al., 2017). Researchers have also developed an improved DSAI approach by using a robust Capon beamformer to reduce the axial elongation artifacts (Coviello et al., 2015). Lastly, DSAI beamforming is well suited for large hemispherical arrays since the spatial resolution increases with the aperture size of the imaging array (Jones et al., 2015).

Future work will explore the feasibility of this technique for non-MRI conformation of BBB opening, along with guidance and monitoring. Passive cavitation imaging with DAS beamforming will be performed in real-time to produce power cavitation images that quantify acoustic cavitation dose. A parametric study will be carried out at varying doses to determine if this method can accurately predict the onset of BBB opening. In addition to power cavitation images, the cavitation signal (i.e. pixel brightness over time) will be analyzed to calculate the amount of cavitation at different flow velocities in a manner similar

to color Doppler imaging. This should allow for discrimination of acoustic cavitation activity in different vasculature components and help identify which acoustic cavitation flow speeds contribute the most to BBB opening. Lastly, the clinical potential of this technique will be investigated using an USgFUS system more suited for transcranial application. This will entail FUS and imaging array components with lower frequencies for adequate transmission and reception across the human skull (Deffieux and Konofagou, 2010). Spatiotemporal clutter filtering methods will be developed for performing power cavitation imaging with FUS and imaging frequencies that overlap. The overall goal is to develop a stand-alone USgFUS system that can target, open, and verify opening of the BBB without the need of contrast-enhanced MRI.

## 5. Conclusions

Passive cavitation imaging with resolution comparable to B-mode ultrasound is possible for pulsed FUS therapies. This relies on the ability to use short FUS pulses with synchronous transmit and receive sequences. Further improvement of image resolution can be achieved by using an imaging array whose frequency bandwidth is above the FUS frequency. This isolates higher frequency components of the acoustic cavitation emissions and reduces sensitivity towards tissue scattering. Passive cavitation image sets acquired at high-frame rates can be processed in a manner similar to power Doppler imaging. In this case, the power cavitation image is proportional to the number and magnitude of acoustic cavitation events in the focal area over time. Power cavitation imaging revealed the distribution of acoustic cavitation activity in the underlying microvasculature during BBB opening with FUS and microbubbles. Regions of BBB opening denoted by contrast-enhanced MRI images were correlated with power cavitation images. This technique shows promise for guidance and monitoring of acoustic cavitation-based FUS therapies.

## Supplementary Material

Refer to Web version on PubMed Central for supplementary material.

## Acknowledgments

This work was supported in part by the National Institutes of Health (NIH) grants R01AG038961 and R01EB009041.

## References

- Ammi A, Cleveland R, Mamou J, Wang G, Bridal S, O'Brien W. Ultrasonic contrast agent shell rupture detected by inertial cavitation and rebound signals. *IEEE Trans Ultrason Ferroelectr Freq Control*. 2006; 53(1):126–136. [PubMed: 16471439]
- Arnal B, Baranger J, Demene C, Tanter M, Pernot M. In vivo real-time cavitation imaging in moving organs. *Phys Med Biol*. 2017; 62(2):843–857. [PubMed: 28072580]
- Arvanitis C, Clement G, McDannold N. Transcranial assessment and visualization of acoustic cavitation: modeling and experimental validation. *IEEE Trans Med Imaging*. 2015; 34(6):1270–1281. [PubMed: 25546857]
- Arvanitis C, Crake C, McDannold N, Clement G. Passive acoustic mapping with the angular spectrum method. *IEEE Trans Med Imaging*. 2017; 36(4):989–993.

- Arvanitis C, Livingston M, Vykhotseva N, McDannold N. Controlled ultrasound-induced blood-brain barrier disruption using passive acoustic emissions monitoring. *PLoS One*. 2012; 7(9):e45783. [PubMed: 23029240]
- Arvanitis C, Livingstone M, McDannold N. Combined ultrasound and MR imaging to guide focused ultrasound therapies in the brain. *Phys Med Biol*. 2013; 58(14):4749–4761. [PubMed: 23788054]
- Arvanitis C, McDannold N. Integrated ultrasound and magnetic resonance imaging for simultaneous temperature and cavitation monitoring during focused ultrasound therapies. *Med Phys*. 2013; 40(11):112901. [PubMed: 24320468]
- Bader K, Haworth K, Maxwell A, Holland C. Post hoc analysis of passive cavitation imaging for classification of histotripsy-induced liquefaction in vitro. *IEEE Trans Med Imaging*. 2017 Epub ahead of print.
- Baseri B, Choi J, Tung Y, Konofagou E. Multi-modality safety assessment of blood-brain barrier opening using focused ultrasound and definity microbubbles: a short-term study. *Ultrasound Med Biol*. 2010; 36(9):1445–1459. [PubMed: 20800172]
- Choi J, Carlisle R, Coviello C, Seymour L, Coussios C. Non-invasive and real-time passive acoustic mapping of ultrasound-mediated drug delivery. *Phys Med Biol*. 2014; 59(17):4861–4877. [PubMed: 25098262]
- Choi J, Coussios C. Spatiotemporal evolution of cavitation dynamics exhibited by flowing microbubbles during ultrasound exposure. *J Acoust Soc Am*. 2012; 132(5):3538–3549. [PubMed: 23145633]
- Choi J, Pernot M, Brown T, Small S, Konofagou E. Spatio-temporal analysis of molecular delivery through the blood-brain barrier using focused ultrasound. *Phys Med Biol*. 2007; 52(18):5509–5530. [PubMed: 17804879]
- Thomas J, Dayton P, May D, Ferrara K. Nondestructive subharmonic imaging. *IEEE Trans Ultrason Ferroelectr Freq Control*. 2002; 49(7):883–892. [PubMed: 12152942]
- Coviello C, Kozick R, Choi J, Gyöngy M, Jensen C, Smith P, Coussios C. Passive acoustic mapping utilizing optimal beamforming in ultrasound therapy monitoring. *J Acoust Soc Am*. 2015; 137(5):2573–2585. [PubMed: 25994690]
- Crake C, Meral F, Burgess M, Papademetriou I, McDannold N, Porter T. Combined passive acoustic mapping and magnetic resonance thermometry for monitoring phase-shift nanoemulsion enhanced focused ultrasound therapy. *Phys Med Biol*. 2017; 62(15):6144–6163. [PubMed: 28590938]
- Crake C, Victor M, Owen J, Coviello C, Collin J, Coussios C, Stride E. Passive acoustic mapping of magnetic microbubbles for cavitation enhancement and localization. *Phys Med Biol*. 2015; 60(2):785–806. [PubMed: 25564961]
- Deffieux T, Konofagou E. Numerical study of a simple transcranial focused ultrasound system applied to blood-brain barrier opening. *IEEE Trans Ultrason Ferroelectr Freq Control*. 2010; 57(12):2637–2653. [PubMed: 21156360]
- Demené C, Deffieux T, Pernot M, Osmanski B, Biran V, Gennisson L, Bergel A, Franqui S, Correas J, Cohen I, Baud O, Tanter M. Spatiotemporal clutter filtering of ultrafast ultrasound data highly increases doppler and fUltrasound sensitivity. *IEEE Trans Med Imaging*. 2015; 34(11):2271–2285. [PubMed: 25955583]
- Downs M, Buch A, Sierra C, Karakatsani M, Teichert T, Chen S, Konofagou E, Ferrera V. Long-term safety of repeated blood-brain barrier opening via focused ultrasound with microbubbles in non-human primates performing a cognitive task. *PLoS One*. 2015; 10(6):e0130860. [PubMed: 26087322]
- Farny C, Holt R, Roy R. Temporal and spatial detection of HIFU-induced inertial and hot-vapor cavitation with a diagnostic ultrasound system. *Ultrasound Med Biol*. 2009; 35(4):603–615. [PubMed: 19110368]
- Feshitan J, Chen C, Kwan J, Borden M. Microbubble size isolation by differential centrifugation. *J Colloid Interface Sci*. 2009; 329(2):316–324. [PubMed: 18950786]
- Gateau J, Aubry J, Pernot M, Fink M, Tanter M. Combined passive detection and ultrafast active imaging of cavitation events induced by short pulses of high-intensity ultrasound. *IEEE Trans Ultrason Ferroelectr Freq Control*. 2011; 58(3):517–532. [PubMed: 21429844]

- Gessner R, Frederick C, Foster F, Dayton P. Acoustic angiography: a new imaging modality for assessing microvasculature architecture. *Int J Biomed Imaging*. 2013; 2013(936593)
- Gyöngy M, Arora M, Noble J, Coussios C. Use of passive arrays for characterization and mapping of cavitation activity during HIFU exposure. *IEEE Ultrasonics Symp (Beijing)*. 2008:871–874.
- Gyöngy M, Coussios C. Passive cavitation mapping for localization and tracking of bubble dynamics. *J Acoust Soc Am*. 2010a; 128(4):EL175–EL180. [PubMed: 20968322]
- Gyöngy M, Coussios C. Passive spatial mapping of inertial cavitation during HIFU exposure. *IEEE Trans Ultrason Ferroelectr Freq Control*. 2010b; 57(1):48–56.
- Haworth K, Bader K, Rich K, Holland C, Mast T. Quantitative frequency-domain passive cavitation imaging. *IEEE Trans Ultrason Ferroelectr Freq Control*. 2017; 64(1):177–191. [PubMed: 27992331]
- Haworth K, Mast T, Radhakrishnan K, Burgess M, Kopechek J, Huang S, McPherson D, Holland C. Passive imaging with pulsed ultrasound insonations. *J Acoust Soc Am*. 2012; 132(1):544–553. [PubMed: 22779500]
- Haworth K, Raymond J, Radhakrishnan K, Moody M, Huang S, Peng T, Shekhar H, Klegerman M, Kim H, McPherson D, Holland C. Trans-stent B-mode ultrasound and passive cavitation imaging. *Ultrasound Med Biol*. 2016; 42(2):518–527. [PubMed: 26547633]
- Haworth K, Salgaonkar V, Corregan N, Holland C, Mast T. Using passive cavitation images to classify high-intensity focused ultrasound lesions. *Ultrasound Med Biol*. 2015; 41(9):2420–2434. [PubMed: 26051309]
- Hilgenfeldt S, Lohse D, Zomack M. Response of bubbles to diagnostic ultrasound: a unifying theoretical approach. *Eur Phys J B*. 1998; 4:247–255.
- Hu X, Zheng H, Kruse D, Stuclicke P, Stephens D, Ferrara K. A sensitive TLRH targeted imaging technique for ultrasonic molecular imaging. *IEEE Trans Ultrason Ferroelectr Freq Control*. 2014; 61(5):870–880. [PubMed: 24801226]
- Hynynen K. MRIgHIFU: a tool for image-guided therapeutics. *J Magn Reson Imaging*. 2011; 34(3): 482–492. [PubMed: 22896850]
- Hynynen K, McDannold N, Vykhodtseva N, Jolesz FA. Noninvasive MR imaging-guided focal opening of the blood-brain barrier in rabbits. *Radiology*. 2001; 220(3):640–646. [PubMed: 11526261]
- Jones R, O'Reilly M, Hynynen K. Experimental demonstration of passive acoustic imaging in the human skull cavity using ct-based aberration corrections. *Med Phys*. 2015; 42(7):4385–4400. [PubMed: 26133635]
- Kruse D, Ferrara K. A new imaging strategy using wideband transient response of ultrasound contrast agents. *IEEE Trans Ultrason Ferroelectr Freq Control*. 2005; 52(8):1320–1329. [PubMed: 16245601]
- Kwan J, Myers R, Coviello C, Graham S, Shah A, Stride E, Carlisle R, Coussios C. Ultrasound-propelled nanocups for drug delivery. *Small*. 2015; 11(39):5305–5314. [PubMed: 26296985]
- Leinenga G, Götz J. Scanning ultrasound removes amyloid- $\beta$  and restores memory in an alzheimer's disease mouse model. *Sci Transl Med*. 2015; 7(278):278ra33.
- Leinenga G, Langton C, Nisbet R, Götz J. Ultrasound treatment of neurological diseases - current and emerging applications. *Nat Rev Neurol*. 2016; 12(3):161–174. [PubMed: 26891768]
- Ma J, Martin K, Dayton P, Jiang X. A preliminary engineering design of intravascular dual-frequency transducers for contrast-enhanced acoustic angiography and molecular imaging. *IEEE Trans Ultrason Ferroelectr Freq Control*. 2014; 61(5):870–880. [PubMed: 24801226]
- Mace E, Montaldo G, Osmanski B, Cohen I, Fink M, Tanter M. Functional ultrasound imaging of the brain: theory and basic principles. *IEEE Trans Ultrason Ferroelectr Freq Control*. 2013; 60(3): 492–506. [PubMed: 23475916]
- Montaldo G, Tanter M, Bercoff J, Benech N, Fink M. Coherent plane-wave compounding for very high frame rate ultrasonography and transient elastography. *IEEE Trans Ultrason Ferroelectr Freq Control*. 2009; 56(3):489–506. [PubMed: 19411209]
- Norton S, Won I. Time exposure acoustics. *IEEE Trans Geosci Remote Sens*. 2000; 38(3):1337–1343.

- O'Reilly M, Hynynen K. Blood-brain barrier: real-time feedback-controlled focused ultrasound disruption by using an acoustic emissions-based controller. *Radiology*. 2012; 263(1):96–106. [PubMed: 22332065]
- O'Reilly M, Jones R, Hynynen K. Three-dimensional transcranial ultrasound imaging of microbubble clouds using a sparse hemispherical array. *IEEE Trans Biomed Eng*. 2014; 61(4):1285–1294. [PubMed: 24658252]
- Pouliopoulos A, Li C, Tinguely M, Garbin V, Tang M, Choi J. Rapid short-pulse sequences enhance the spatiotemporal uniformity of acoustically driven microbubble activity during flow conditions. *J Acoust Soc Am*. 2015; 140(4):2469–2480.
- Salgaonkar V, Datta S, Holland C, Mast T. Passive cavitation imaging with ultrasound arrays. *J Acoust Soc Am*. 2009; 126(6):3071–3083. [PubMed: 20000921]
- Simpson D, Chin C, Burns P. Pulse inversion Doppler: a new method for detecting nonlinear echoes from microbubble contrast agents. *IEEE Trans Ultrason Ferroelectr Freq Control*. 1999; 46(2): 372–382. [PubMed: 18238434]
- Sun T, Samiotaki G, Wang S, Acosta C, Chen C, Konofagou E. Acoustic cavitation-based monitoring of the reversibility and permeability of ultrasound-induced blood-brain barrier opening. *Phys Med Biol*. 2015; 60(23):9079–9094. [PubMed: 26562661]
- Sun T, Zhang Y, Power C, Alexander P, Sutton J, Aryal M, Vykhodtseva N, Miller E, McDannold N. Closed-loop control of targeted ultrasound drug delivery across the blood-brain/tumor barriers in a rat glioma model. *Proc Natl Acad Sci USA*. 2017; 114(48):E10281–E10290. [PubMed: 29133392]
- Timbie K, Mead B, Price R. Drug and gene delivery across the blood-brain barrier with focused ultrasound. *J Control Release*. 2015; 219:61–75. [PubMed: 26362698]
- Tsai C, Zhang J, Liao Y, Liu H. Real-time monitoring of focused ultrasound blood-brain barrier opening via subharmonic acoustic emission detection: implementation of confocal dual-frequency piezoelectric transducers. *Phys Med Biol*. 2016; 61(7):2926–2946. [PubMed: 26988240]
- Tung Y, Vlachos F, Feshitan J, Borden M, Konofagou E. The mechanism of interaction between focused ultrasound and microbubbles in blood-brain barrier opening in mice. *J Acoust Soc Am*. 2011; 130(5):3059–3067. [PubMed: 22087933]
- Wei K, Tsai H, Lu Y, Yang H, Hua M, Wu M, Chen P, Huang C, Yen T, Liu H. Neuronavigation-guided focused ultrasound-induced blood-brain barrier opening: a preliminary study in swine. *AJNR Am J Neuroradiol*. 2013; 34(1):115–120. [PubMed: 22723060]
- Wu S, Tung Y, Marquet F, Downs M, Sanchez C, Chen C, Ferrera V, Konofagou E. Transcranial cavitation detection in primates during blood-brain barrier opening - a performance assessment study. *IEEE Trans Ultrason Ferroelectr Freq Control*. 2014; 61(6):966–978. [PubMed: 24859660]

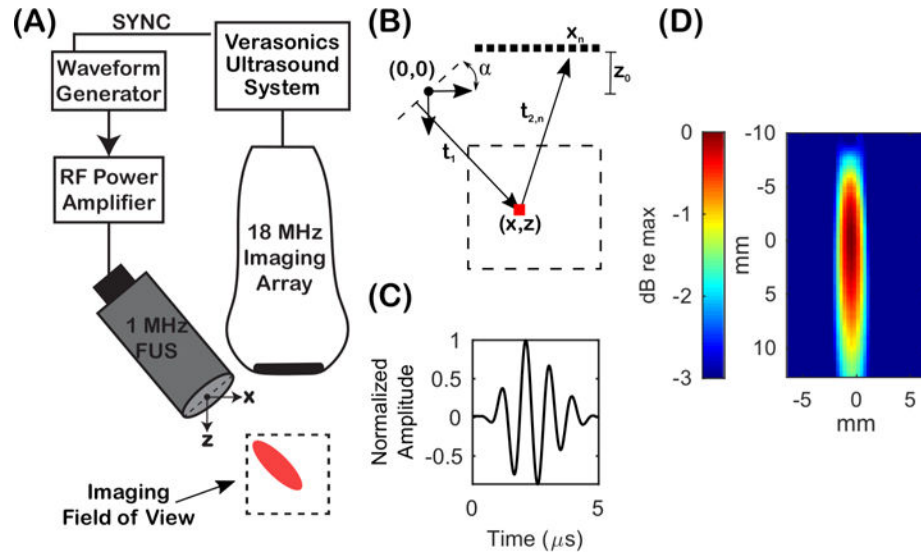


**Figure 1.**

(A) Experimental setup for performing passive cavitation imaging. A 1-MHz focused ultrasound (FUS) transducer was aligned off-axis relative to an 18-MHz imaging array. The imaging array was operated in a receive-only mode and the FUS transducer was used to transmit therapy pulses. A Verasonics research ultrasound system was used to synchronize the FUS transmit and receive acquisition of the imaging array. (B) Image geometry for calculating time delays prior to beamforming. (C) Transmit waveform of the 1-MHz FUS transducer. (D) Axial beamplot of the 1-MHz transducer.

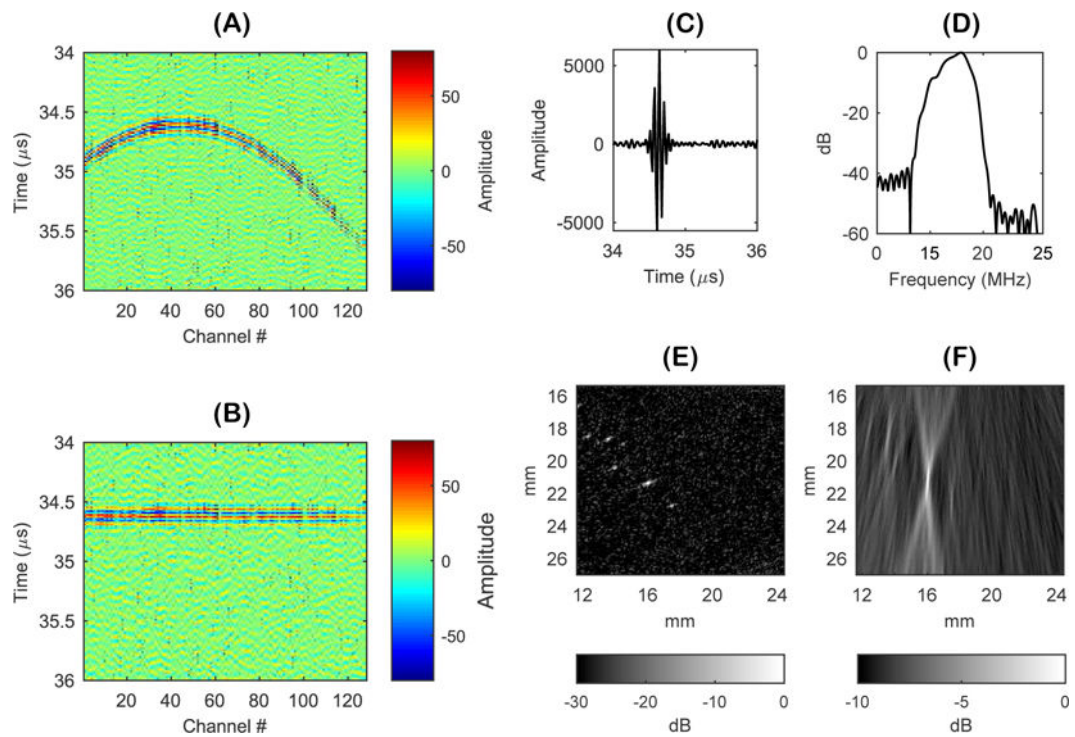


**Figure 2.**

(A) Received radio frequency (RF) data from the strongest microbubble source located at a (x,z) coordinate of (16 mm, 21 mm). (B) Delayed received RF data. (C) Delayed and summed (beamformed) RF signal for the pixel located at the strongest microbubble source. (D) Power spectrum of beamformed RF signal. (E) Passive cavitation image using delay and sum beamforming (DAS) with absolute time delays. (F) Passive cavitation image using delay, sum, and integrate (DSAI) beamforming with relative time delays.

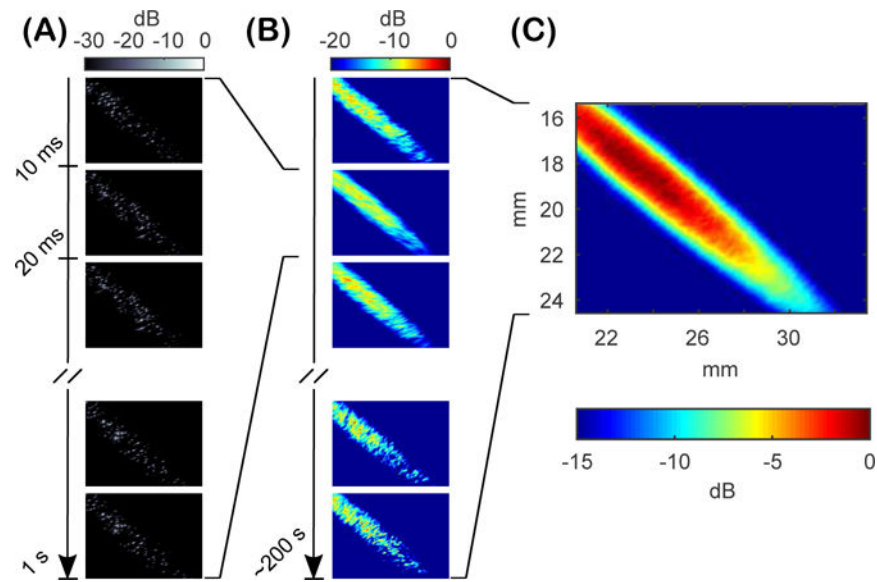


**Figure 3.** Free-field passive cavitation imaging of a microbubble suspension. (A) High-frame rate (100 Hz) acquisition of 100 frames of passive cavitation images processed using delay and sum (DAS) beamforming with absolute time delays. (B) Individual power cavitation images from each 100 frame set of passive cavitation images acquired approximately every second. (C) The mean power cavitation image produced from 100 frames of power cavitation images (10,000 frames of passive cavitation images).

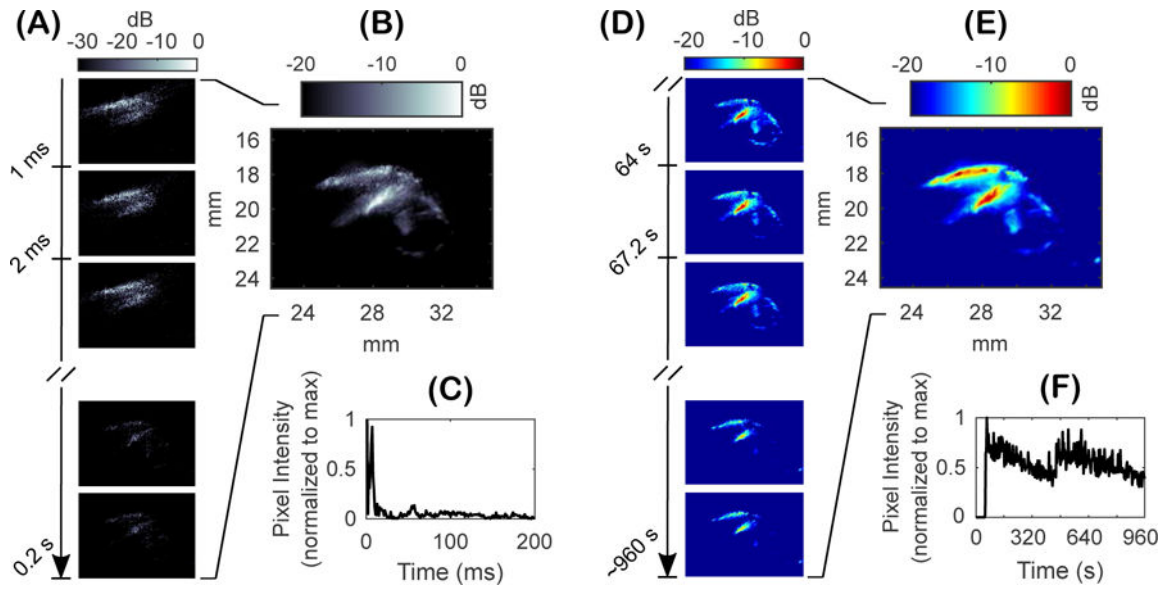


**Figure 4.** *In vivo* monitoring of acoustic cavitation with passive cavitation imaging during blood-brain barrier (BBB) opening with focused ultrasound (FUS) and microbubbles. (A) High-frame rate (1000 Hz) acquisition of a 200 frame set of synchronous passive cavitation images processed using delay and sum (DAS) beamforming with absolute time delays. (B) Power cavitation image for the 200 frame set of passive cavitation images. (C) Pixel intensity over time for the set passive cavitation images at a (x,z) coordinate of (28 mm, 18 mm). (D) Individual power cavitation images from each 200 frame set of passive cavitation images acquired approximately every three seconds over the entire treatment duration. (E) The mean power cavitation image produced from 300 frames of power cavitation images. (F) Pixel intensity of the power cavitation image set at a (x,z) coordinate of (28 mm, 19.5 mm) over the treatment duration.

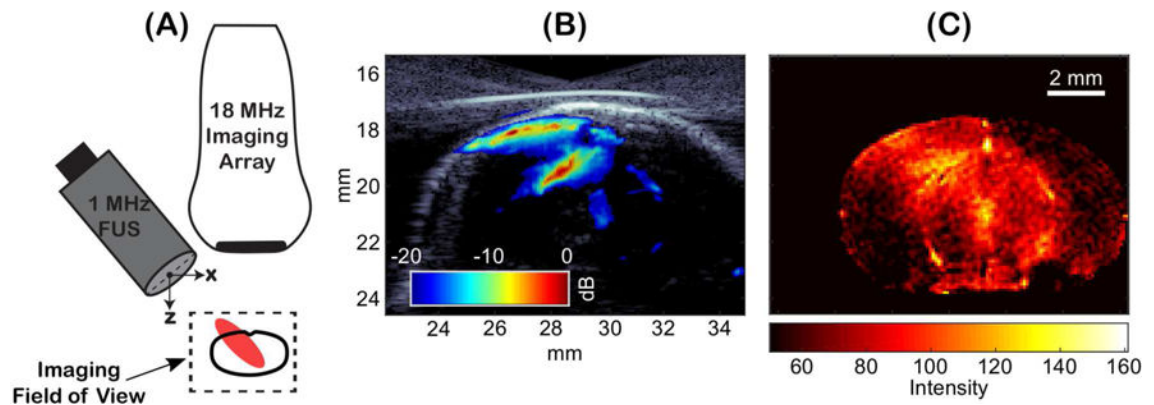


**Figure 5.**

(A) Schematic showing the alignment of the focal area (denoted in red) and mouse brain (outlined in black). (B) Overlay of the B-mode and mean power cavitation images captured with the 18-MHz imaging array. (C) Contrast-enhanced MRI after focused ultrasound (FUS)-mediated blood-brain barrier (BBB) opening with microbubbles showing BBB opening (denoted by increased pixel intensity) along the path of FUS propagation.